Experimental and numerical investigation of the mechanism of drag reduction by surfactant additives and heat transfer

Yasuo Kawaguchi[1], Feng-Chen Li[1,3], Yu Bo[1,3] and Koichi Hishida[2]

1. Turbomachinery Group, Energy Technology Research Institute,
National Institute of Advanced Industrial Science and Technology (AIST),
Namiki 1-2-1, Tsukuba 305-8564, Japan
2. Department of System Design Engineering, Keio University,
Yokohama, 223-8522, Japan
3. Center for Smart Control of Turbulence
Email: kawaguchi.y@aist.go.jp

Abstract

In this article we summarized the principal results of our experimental and numerical studies on the characteristics of turbulence structures, turbulence transport for momentum and heat in a drag-reduced turbulent channel flow with surfactant additives. Particle image velocimetry (two-dimensional and stereoscopic) was employed to investigate turbulence structures and momentum transport and laser Doppler velocimetry combining with a fine-wire thermocouple was used to investigate turbulence transport for heat. The numerical study was performed by using DNS. The combination of experimental and numerical results shed light upon the mechanisms of drag reduction and heat transfer reduction in surfactant solution flows.

1. Introduction

Some kinds of surfactant have great effectiveness in reducing skin-friction drag in a wall-bounded turbulent water flow. After adding such surfactant to turbulent water flow, even the mass concentration is merely of the order of tens to thousands per million, up to 90% skin-friction drag may be reduced at the same flow rate (Zakin et al. 1997). This phenomenon has significant potentials in saving energy in the industrial applications, such as in saving pumping power of a long-distance water-circulating system. The drag-reducing ability of surfactant solution depends upon fluid temperature, solution concentration, counterion and its concentration, solvent quality, flow passage configuration and flow rate or Reynolds number (Re). In essence, it is generally believed that the drag-reducing ability arises because of viscoelasticity of solution flow imparted by the so-called shear induced structure (SIS), since the surfactant molecules, with addition of certain counterions, can form rod-like micelles and then network structures (SIS) under a certain range of shear stress (Zakin et al. 1997, Lu et al. 1998, Hu and Matthys 1997, Hu et al. 1998a,b). On the other hand, in the application of drag-reducing surfactants to a water-circulating system with heat exchanger, such as a district heat/cooling system the heat transfer problem is inevitably encountered because heat transfer reduction (HTR), at similar or even higher level compared with drag reduction (DR), also occurs due to the dramatic turbulence suppression. The abovementioned complexities call for, from the viewpoint of industrial flow-control as well as physics, a comprehensive understanding of the characteristics of turbulence structure influenced by drag-reducing additives and mechanisms of DR and HTR is necessary before surfactant drag reducers are put to practical and effective use.

Our research group has been carrying out experimental and numerical studies on the issues of drag-reducing channel flow with surfactant additives (Li et al. 2001a,b, Kawaguchi et al. 2002, Yu and Kawaguchi 2003, 2004, Yu et al. 2004, Li et al. 2004a,b,c,d,e,f). In the part of experimental study of this article, we reviewed the recent experimental studies, by means of modern laser techniques, on the characteristics of turbulence structures, momentum and thermal turbulence transport in drag-reduced flows by surfactant additives (Li et al. 2004a,b,c,d,e,f). In these studies, laser Doppler velocimetry (LDV) combing with a fine-wire thermocouple (TC) probe were used to measure turbulent velocity and temperature fluctuations simultaneously so as to obtain the characteristic terms of thermal turbulence transport in a turbulent flow; particle image velocimetry (PIV) was employed to measure the two-dimensional (2D) and 2D-three component (2D-3C, by stereoscopic PIV) turbulent velocity fields in the streamwise-wall-normal, streamwise-spanwise, spanwise-wall-normal planes respectively in order to investigate the detailed turbulent vortex structures influenced by drag-reducing surfactant additives in a wall- bounded turbulent flow.

In the part of numerical study, we have been studying the drag-reducing flow by surfactant additives for

four-years and the research outcomes are summarized as follows. Giesekus model was found to be a suitable model to describe the rheological properties of the drag-reducing flow and was adopted to simulate the drag-reducing phenomena. A faithful finite-difference scheme was proposed for the drag-reducing viscoelastic flow. The numerical and experimental results for a 75 ppm CTAC surfactant solution are in good agreement. The heat transfer reduction is qualitatively simulated. The effects of rheological parameters on the drag-reduction were studied. A bi-layer model was proposed and the effectiveness region of the surfactant additives were confirmed by this simple model.

2. Experimental Study

2.1 Experimental Facility

The flow system is schematically shown in Fig. 1. The 2D channel was made of transparent acrylic resin and had a length of 10 m, height (H) of 0.04 m and width of 0.5 m. A 0.15 m long honeycomb rectifier was set at the channel entrance for removing large eddies. An electromagnetic flow meter with uncertainty of ±0.01 m^3/min was installed upstream of the channel for measuring flow rate. The reservoir in the flow loop contained cooling coils and a heater, which were for maintaining a constant fluid temperature. The wall shear stress was estimated from the static pressure gradient measured with pressure tabs located on the bottom wall of the channel over a certain distance with uncertainty of ±0.1 Pa. The drag-reducing fluid flow was an aqueous solution of CTAC/NaSal system (CTAC and NaSal had same weight-concentration), where CTAC represents cationic surfactant cetyltrimethyl ammonium chloride and NaSal stands for sodium salicylate. The flow conditions are shown in Table 1.

2.2 Methods

The characteristics of turbulence structures in a drag-reduced flow were studied through investigating the 2D and 2D-3C turbulent velocity fields measured with conventional PIV and stereoscopic PIV respectively. The optical configuration for PIV measurements is shown in Fig. 2. 2D velocity field was measured in the streamwise-wall-normal (x-y) plane and 2D-3C velocity fields were measured in the streamwise-spanwise (x-z) plane and wall-normal- spanwise (y-z) plane respectively. T he measurement position was located at 7.0 m (175H) downstream of the channel entrance.

LDV combining with a fine-wire TC probe was used to measure turbulent velocity and temperature fluctuations simultaneously. Figure 3 shows the diagram of test section and locations of LDV measurement volume and TC probe. This measurement position was located at 9.0 m (225H) downstream of channel entrance. The characteristics of turbulent heat transfer affected by drag-reducing additives were studied based on the simultaneous data set of fluctuations of velocity and temperature, u, v and θ.

2.3 Results of experimental study

2.3.1 Quantitative relationship between turbulent bursting events and skin friction (Li et al. 2004e)

The near-wall coherent vortex structures (vortex packets) are directly associated with turbulent bursting events, i.e. ejection motion of low-momentum fluids from the wall and sweep motion of high-momentum fluids toward the wall (Fig. 4). Hence we use the spatial and configurational parameters of coherent vortex structures to characterize bursting events: gradient of the ramp-shaped low momentum region confined by the vortex cores of a vortex packet stands for the strength of a bursting event and the spatial frequency stands for the temporally occurring frequency of bursts. As shown in Fig. 4, the near-wall coherent structures are extracted from 200 frames of velocity field obtained in the x-y plane for water flow and drag-reduced flows respectively, and inclination angle (γ) of the low-momentum region and spatial frequency ($n = N/(2\Delta L)$, where N is number of the extracted coherent structures and ΔL is length of the measured range in the x direction) of such structures are measured. Figure 5 shows the profiles of measured Reynolds shear stress for water and drag-reduced flows. The turbulent contribution to friction factor, f_T, is thus calculated by weighted integration of the profile of $-\overline{uv}$. With the obtained f_T, n and $\overline{\gamma}$ (averaged γ), we plot f_T versus $n \cdot \tan(\overline{\gamma})$ for five flows on Fig. 6, showing the quantitative relationship between turbulent bursting events and skin friction factor, i.e., $f_T = A + B \cdot n \cdot \tan(\overline{\gamma})$, where A and B are constants.

2.3.2 Turbulence structures modified by surfactant additives (Li et al. 2004e,f)

Figure 7 demonstrates a snapshot velocity field (Reynolds-decomposed vector with contour map of swirling

stre   ngth) measured in the x-y plane for five flows respectively. It is shown that the vortex structures near the walls in the drag-reducing surfactant solution flow are changed gradually with DR level: the growth angle of vortex packets or inclination angle of the ramp-shaped regions decreases and the appearance of coherent vortex structures becomes less frequent. The instantaneous velocity field and contour map of uv/u_τ^2 for five flows are also visualized. It is seen that *large-amplitude* contributions to uv/u_τ^2 across the channel height only concentrate on several patches where the ejection or sweep motion occurs, and the area of these patches in drag-reduced flows shrinks and the amplitude of uv/u_τ^2 on such patches decreases with DR level. As a consequence of the influence of surfactant additives, the ensemble value $-\overline{uv}$ is decreased, as shown in Fig. 5.

Figure 8 shows a stereoscopic PIV-measured instantaneous velocity field in the x-z plane in a water flow and a CTAC solution flow respectively, demonstrating the most important near-wall turbulence structures closely associated with turbulent bursting events, namely, low-speed streaks and coherent vortex packets. It can be seen that a series of wall-normal vortex cores align with the low-speed streaks with opposite signals of vorticity at both sides of each streak, indicating two essential points: the appearance of hairpin vortex packets and the formation of low-speed streaks due to the hairpin vortex packets. At the low-speed region, the wall-normal velocity component mostly has positive signal, as shown in Fig. 8a ii. Influenced by the drag-reducing surfactant additives, 1) the alignment of the near-wall low-speed streaks becomes relatively regular compared with water flow, indicating a depression of turbulence, 2) the dimension of the streaks broadens in both the spanwise and streamwise directions and 3) the spanwise spacing between the streaks becomes large, as plotted in Fig. 9 in which the distance between the origin and the first positive peak in the spanwise autocorrelation of u, $Corr(u,u)$, is taken as a measure of the spanwise spatial scale: $\Delta z^+ = 190$ in the measured CTAC solution flow compared with $\Delta z^+ = 134$ in water flow.

Figure 10 shows the conditionally averaged velocity field based on local minimum-U event for water and CTAC solution flows. The low-speed region appearing on the conditionally averaged contour map of u more evidently exhibits the lengthening feature of the low-speed streaks in drag-reduced flow. The contour of ω_y^+ (wall-normal vorticity) reveals that the symmetrical counter-rotating vortex pair in the averaged velocity field in CTAC solution flow is elongated in the x direction to a much greater extent than that in water flow, indicating a much smaller inclination angle of vortex tubes or leg(s) of the hairpin vortex in the buffer layer in drag-reduced flow. The clear streamwise swirling motion implied by the contour of v/u_τ as appeared in water flow is ambiguous in CTAC solution flow, and the amplitude of v/u_τ is also greatly decreased in drag-reduced flow. These phenomena provide further evidences of depression of turbulence, namely, weakening of the vortices and turbulent events by the drag-reducing surfactant additives.

An instantaneous 2D-3C velocity field in the y-z plane measured by stereoscopic PIV is demonstrated in Fig. 11 for water and CTAC solution flows respectively. The contour of $\omega_x^+\big|_{\lambda_{ci}}$ (the streamwise vorticity at non-zero-swirling-motion locations) exhibits that many vortex cores distribute across the channel height. In drag-reduced flow, the streamwise vorticity is decreased. While there appear a few of counter-rotating vortex pairs among all in water flow (about 90% of all the measured velocity fields in the y-z plane show only single cores or pairs that are quite asymmetrical), no obvious counter-rotating vortex pair is observed in drag-reducing CTAC solution flow.

PIV system was also employed to clarify the Re-dependence of turbulence structures in a drag-reducing surfactant solution flow (Li et al. 2004d). Presence of a larger diffusivity layer was found near the wall in certain Re number range and concentration of surfactant. This phenomena can be related to the destruction of micellar structure and loss of drag reduction can be explained. The bi-layer analysis based on the this finding was also made (Yu B and Kawaguchi Y, 2004b).

2.3.3 Characteristics of turbulence transport for momentum and heat in a drag-reduced flow (Li et al. 2004a,b,c)

The turbulence production of turbulent kinetic energy, $-\overline{u^+v^+}\left(\partial U^+/\partial y^+\right)$, and of temperature variance, $-\overline{v^+\theta^+}\left(\partial\Theta^+/\partial y^+\right)$, are shown in Fig. 12. The productions of turbulent kinetic energy and temperature variance are reduced in the drag-reducing CTAC solution flows, and the reduction occurred in $-\overline{u^+v^+}\left(\partial U^+/\partial y^+\right)$ is more significant. Figure 5 has shown that the turbulence transport for momentum is greatly depressed in drag-reducing CTAC solution flows, resulting in DR. Figure 13 plots the profiles of the wall-normal turbulent heat flux, illustrating the characteristics of turbulence transport for heat. It is shown that $-\overline{v^+\theta^+}$ is also greatly decreased in drag-reduced flows, which directly causes HTR. Further investigation indicates that the decreases of $-\overline{u^+v^+}$ and $-\overline{v^+\theta^+}$ occur in the same way, namely, the loss of correlation between the two variables in addition to the decrease of v'. The momentum and heat eddy diffusivities, v_t^+ and α_t^+, are shown in Fig. 14. It is found that

both v_t^+ and α_t^+ in drag-reducing CTAC solution flows are decreased across the whole measured range compared with those in water flow, and with the increase of DR and HTR level, the depression of v_t^+ and α_t^+ becomes increasingly significant. Figure 15 shows the turbulent Prandtl number. For the drag-reducing CTAC solution flows, the estimated profiles of Pr_t are quite different from that of water flow: at $y^+ > 50$, the Pr_t profiles are close to that of water flow, but towards the heated wall from 50 wall units at which the mean fluid temperature in CTAC solution flows has larger gradient than in water flow, Pr_t increases until a value close to the molecular Prandtl number for the solution flows.
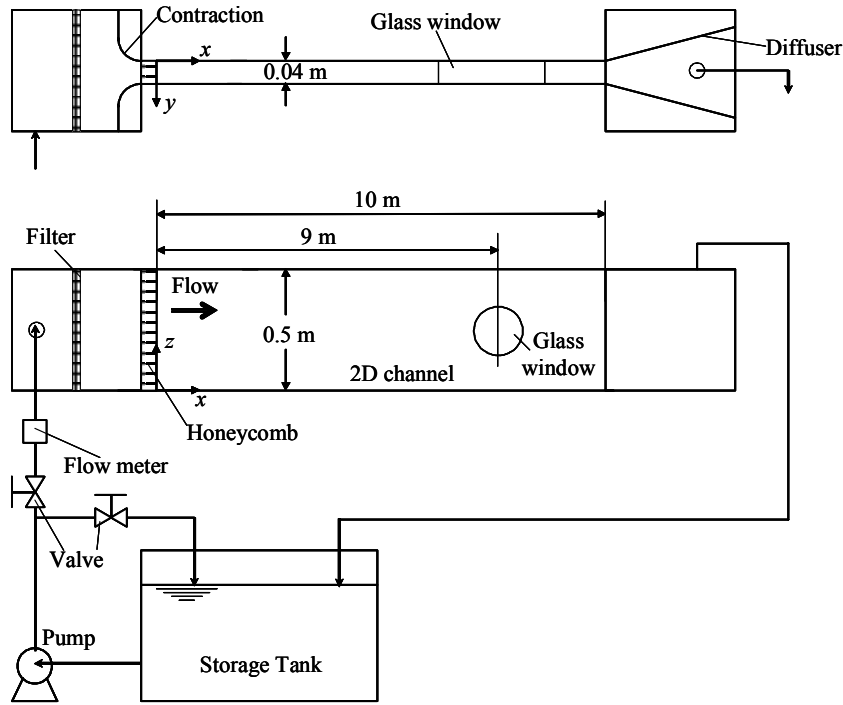
Fig. 1 Schematic diagram of the flow facility

Table 1 Test parameters

Cases		T_{in} (°C)	Re ($\times 10^4$)	u_τ (m/s)	DR (%)
Water flow	W	30	1.8	0.020	-
	Water	25	1.1	0.015	-
	WaterT	31	2.5	0.025	-
CTAC solution flow (25 ppm)	C1	30	2.6	0.026	10
	C2	30	2.1	0.019	34
	C3	30	1.3	0.010	58
CTAC solution flow (30 ppm)	CTAC	25	1.5	0.012	54
	CA	31	3.5	0.027	33
	CB	31	2.5	0.012	70
	CC	31	1.5	0.009	65
CTAC solution flow (75 ppm)	C4	30	1.1	0.009	51

Nd-YAG laser

Flow

2D Channel

Glass window

CCD Camera

H

y

x *z*
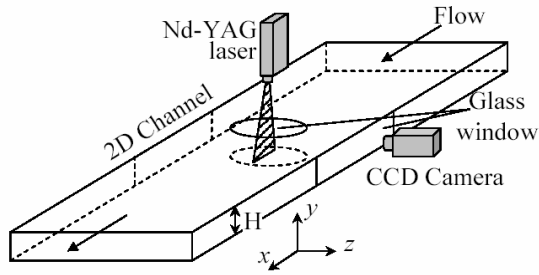
(a) 2D velocity measurement in the x-y plane

Laser sheet   Prism

2D channel

H

y

Camera A   Camera B

flow

y

x *z*

Laser sheet

2D channel

H

Camera A

Prisms

Camera B

flow

y

x *z*
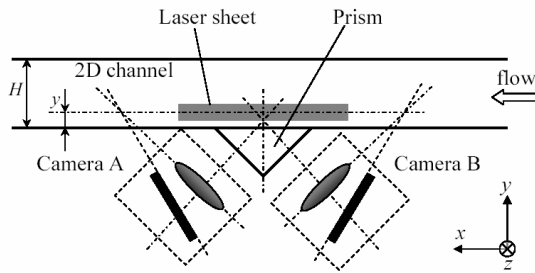
(b) 2D-3C velocity measurement in the x-z plane   *(c) 2D-3C velocity measurement in the y-z plane*
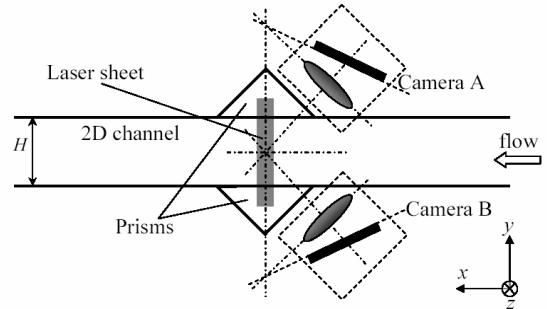
Fig. 2 Optical configurations for PIV measurements.

Measurement position   TC Probe

y

8.2m   0.8m

flow

H = 0.04m   Thermal boundary layer

x

Heating plate

Measurement volume of LDV
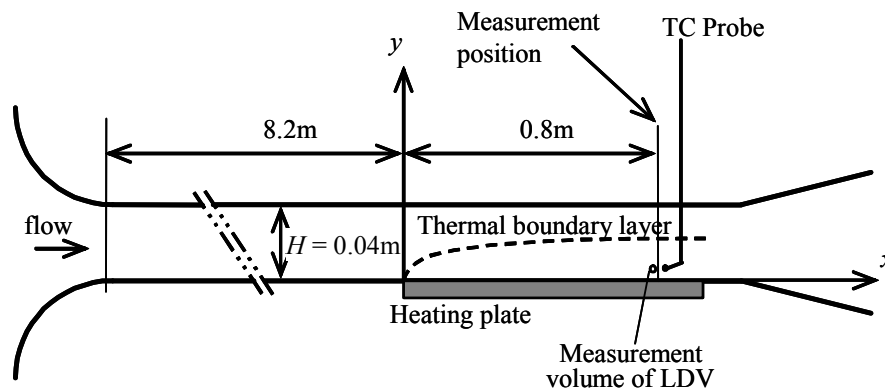
Fig. 3 Schematic diagram of the test section for simultaneous
measurement of velocity and temperature fluctuations (side view).

Sweep   Vortices

flow

20 mm

Ejection

γ

Low-momentum region   Channel wall

42 mm
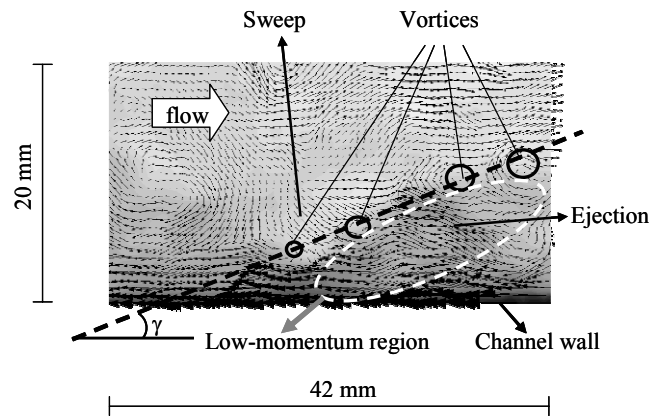
Fig. 4 Near-wall coherent structure in a turbulent channel
flow for the case W. The vector is Reynolds-decomposed u-
v field and contour map is for u.

5
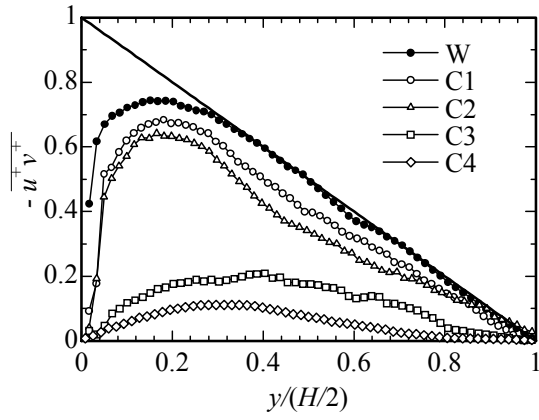
Fig. 5 Profiles of average Reynolds shear stress.
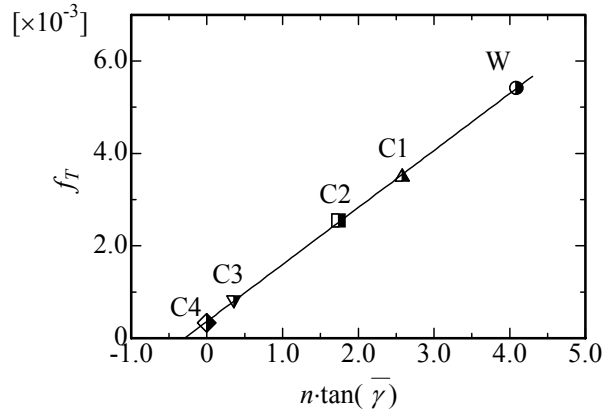
Fig. 6 Turbulent contribution to friction factor as a function of spatial frequency and inclination angle of coherent structures.

(a) W

(b) C1

(c) C2

(d) C3

(e) C4
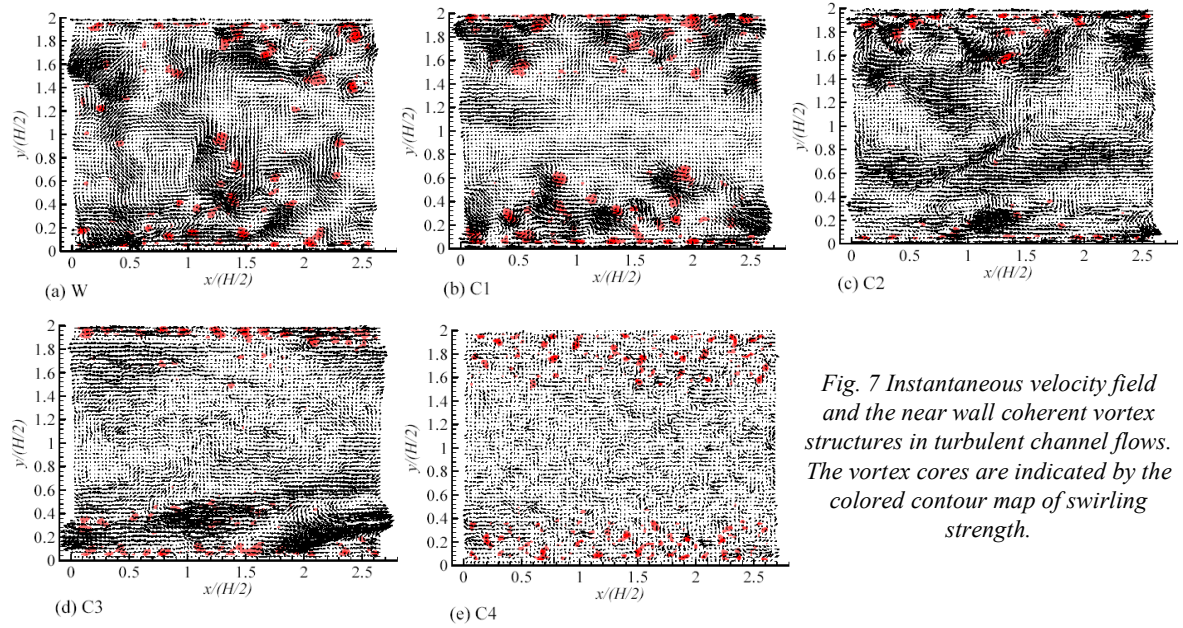
Fig. 7 Instantaneous velocity field and the near wall coherent vortex structures in turbulent channel flows. The vortex cores are indicated by the colored contour map of swirling strength.

(a)

(b)
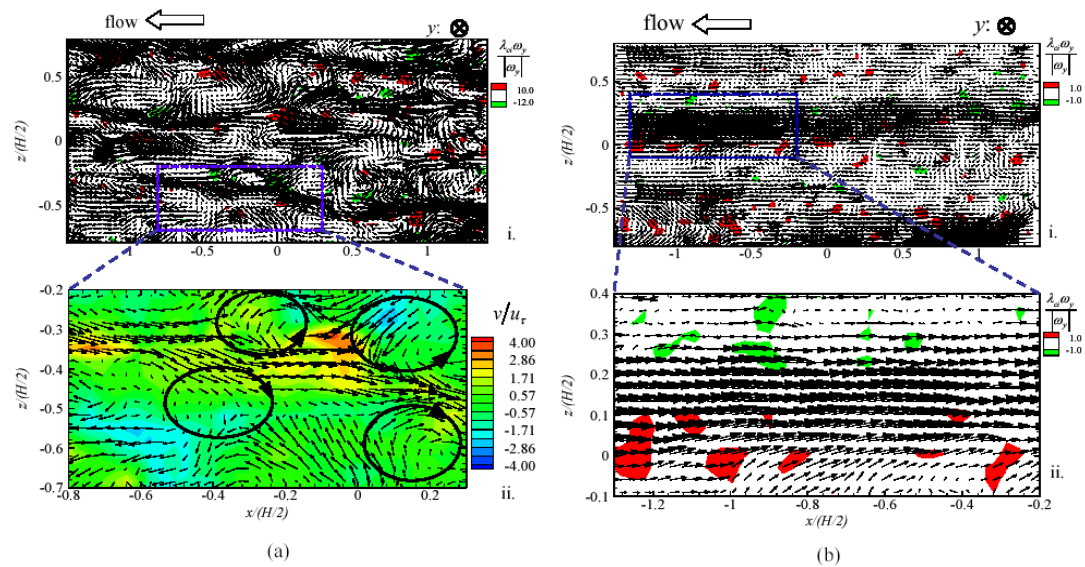
Fig. 8 Instantaneous velocity field in the x-z plane showing the near wall coherent vortex structures in turbulent channel flows. (a) Water at $y^+ = 16.5$ and (b) CTAC at $y^+ = 13.8$. The vortex cores are indicated by the colored contour map of swirling strength in (a) i., (b) i. and (b) ii., and (a) ii. shows the characteristics of wall-normal velocity fluctuation at the low-speed streak region.
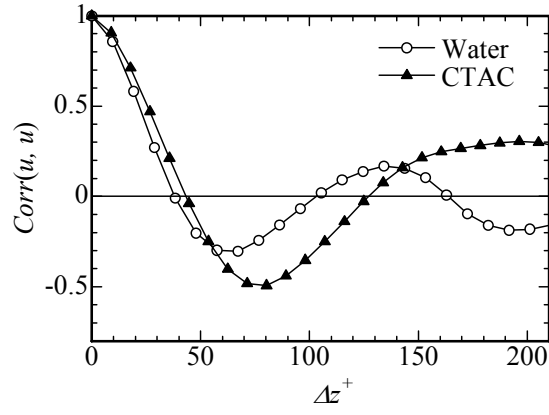
Fig. 9 Autocorrelation of streamwise velocity fluctuations versus spanwise distance for a water flow at $y^+ = 16.5$ and a CTAC solution flow at $y^+ = 13.8$ respectively.

(a)

(b)
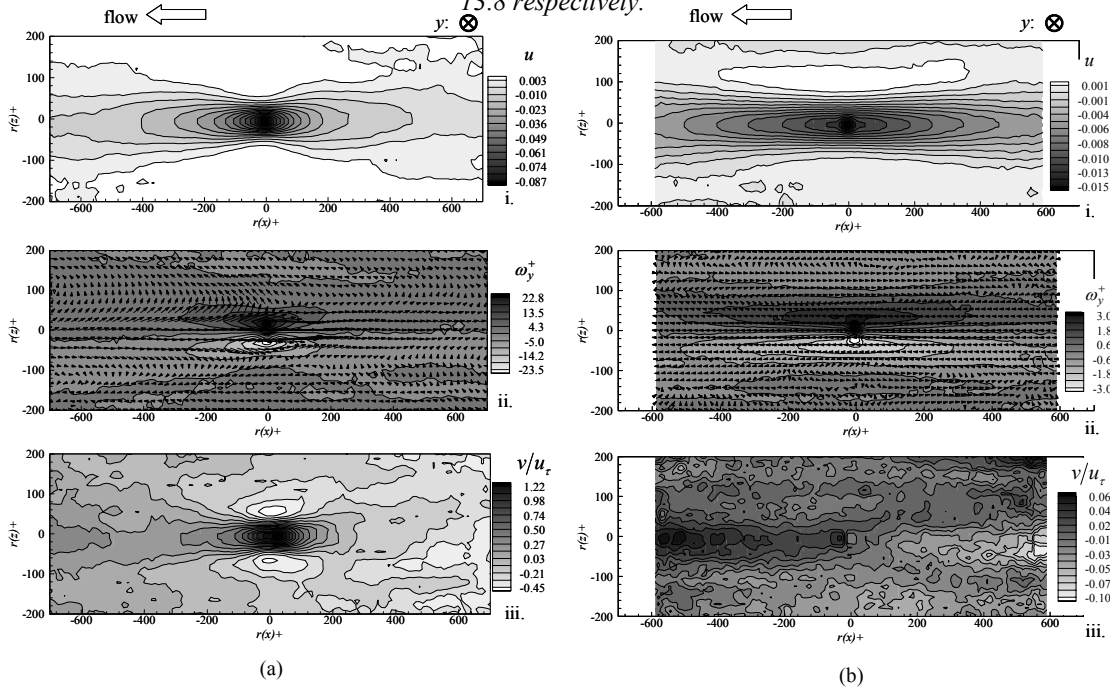
Fig. 10 Conditionally averaged structure in the x-z plane, (a) Water at $y^+ = 16.5$ and (b) CTAC at $y^+ = 13.8$. i. contour of u; ii. velocity vectors with patches of ω_y; iii. contour of v/u_τ

(a)

(b)
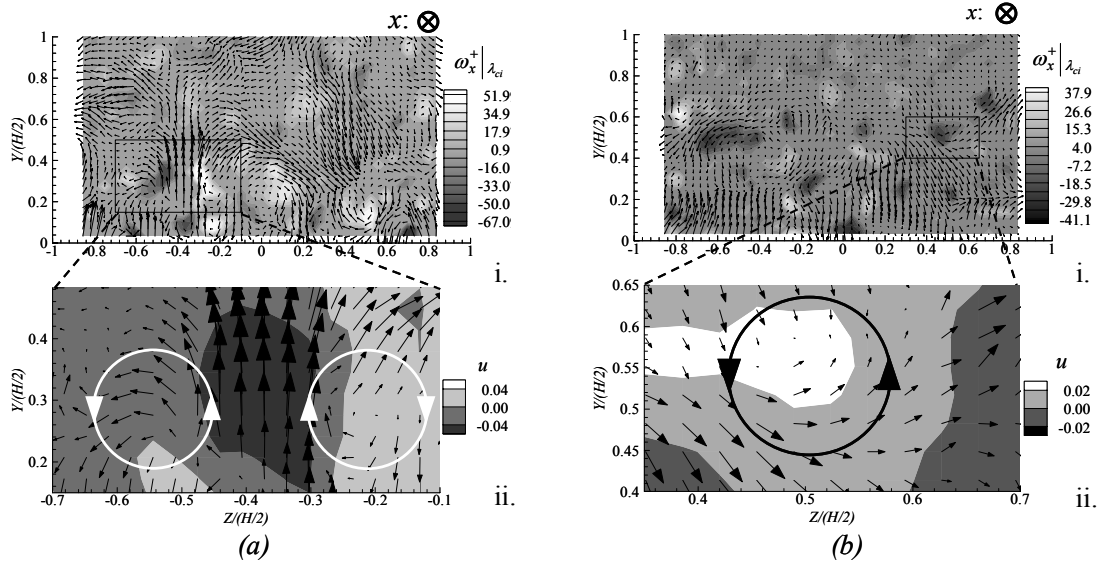
Fig. 11 Instantaneous velocity field in the y-z plane for water flow. (a) Water and (b) CTAC. i. velocity vectors with patches of $\omega_x^+|_{\lambda_{ci}}$ (positive and negative values represent clockwise and counter-clockwise rotations respectively); ii. close view to highlight the vortex pair and ejection motion.

7
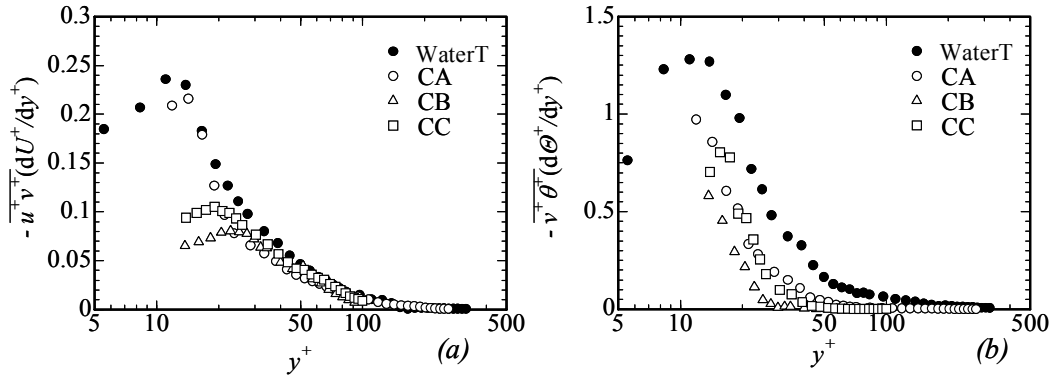
Fig.12 Turbulent productions of turbulent kinetic energy (a) and of temperature variance (b)
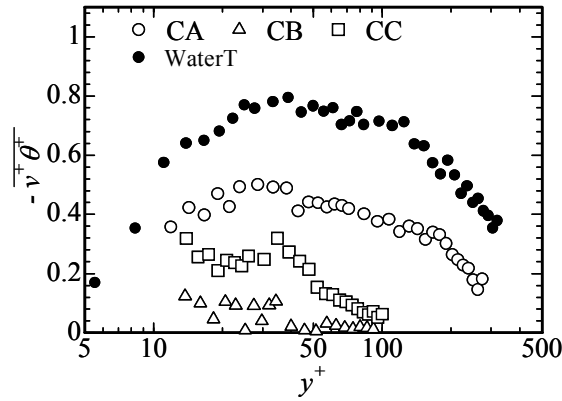
Fig.13 Profiles of the wall-normal turbulent heat flux.
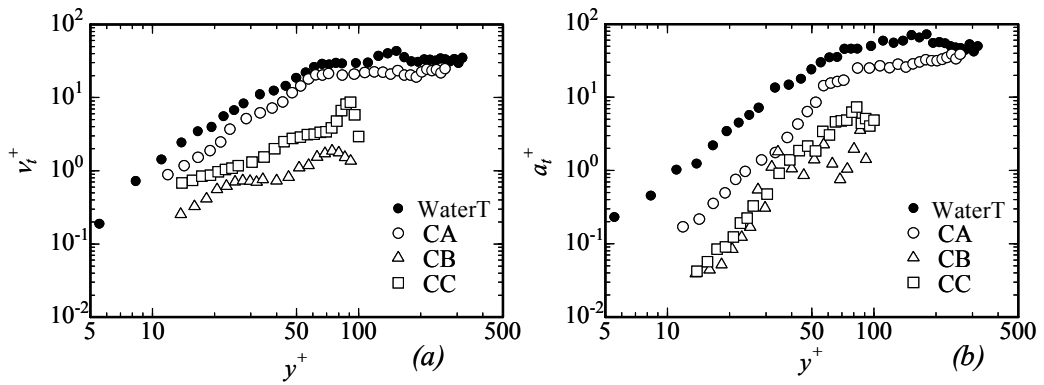
Fig.14 Profiles eddy diffusivity for momentum (a) and heat (b).
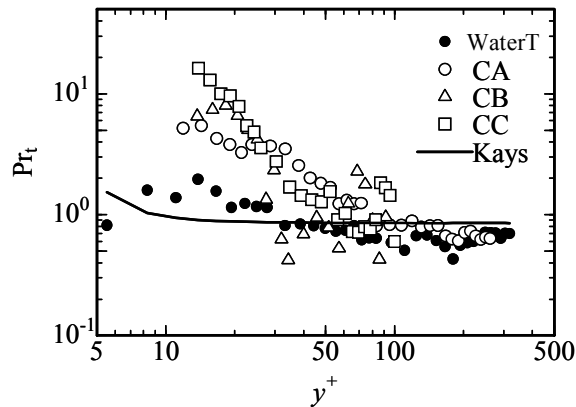
Fig.15 Profiles of the turbulent Prandtl number.

8

3. Numerical Study

3.1 Governing equations and numerical method

The drag-reduction by surfactant additives is related to the elasticity of the network structures formed by the rod-like micelles in the solution. We employed a viscoelastic Giesekus constitutive equation to model the interaction between the elastic network structures and solvent. The dimensionless governing equations for a fully developed turbulent channel flow can be written as:

$$\frac{\partial u_i^+}{\partial x_i^*} = 0 \tag{1}$$

$$\frac{\partial u_i^+}{\partial t^*} + u_j^+ \frac{\partial u_i^+}{\partial x_j^*} = -\frac{\partial p^+}{\partial x_i^*} + \frac{1}{\mathrm{Re}_\tau} \frac{\partial}{\partial x_j^*}\left(\frac{\partial u_i^+}{\partial x_j^*}\right) + \frac{\beta}{\mathrm{We}_\tau} \frac{\partial c_{ij}^+}{\partial x_j^*} + \delta_{1i} \tag{2}$$

$$\frac{\partial c_{ij}^+}{\partial t^*} + \frac{\partial u_m^+ c_{ij}^+}{\partial x_m^*} - \frac{\partial u_i^+}{\partial x_m^*} c_{mj}^+ - \frac{\partial u_j^+}{\partial x_m^*} c_{mi}^+ + \frac{\mathrm{Re}_\tau}{\mathrm{We}_\tau}\left[c_{ij}^+ - \delta_{ij} + \alpha\left(c_{im}^+ - \delta_{im}\right)\left(c_{mj}^+ - \delta_{mj}\right)\right] = 0 \tag{3}$$

In the above equations, c_{ij}^+ is the conformation component associated with the deformation of network microstructure formed by the rod-like micelles in the surfactant solution, and β ($\beta = \eta_a / \eta_s$) is the ratio between the surfactant contribution η_a and solvent contribution η_s to the zero-shear rate viscosity η_0 ($\eta_0 = \eta_a + \eta_s$). The Reynolds number and Weissenberg number are defined as: $\mathrm{Re}_\tau = \rho u_\tau h / \eta_s$ and $\mathrm{We}_\tau = \rho \lambda u_\tau^2 / \eta_s$, where ρ, λ, u_τ and h are the fluid density, relaxation time, friction velocity and half the channel height respectively. Note that the Reynolds number and Weissenberg number are based on the viscosity of solvent. By setting $\beta = 0$, the Navier-stokes equation for a Newtonian fluid is obtained.

The energy equation for the fully-developed turbulent isoflux channel flow is:

$$\frac{\partial \theta^+}{\partial t^*} + u_j^+ \frac{\partial \theta^+}{\partial x_j^*} = \frac{2u^+}{\int_{-1}^{1} U^+ dy} + \frac{1}{\mathrm{Re}_\tau \, \mathrm{Pr}} \frac{\partial}{\partial x_j^*}\left(\frac{\partial \theta^+}{\partial x_j^*}\right) \tag{4}$$

The numerical method used here is a fractional-step method. The Adams-Bashforth scheme is used for time-advancement to ensure second-order accuracy in time. The second-order faithful finite difference scheme of Yu et al. 2004a is used to enhance the numerical stability.   Compared to artificial spectral method (Sureshkumar Beris and Handler 1997), our method has better accuracy and stability .

3.2 Results of nxperimental study

3.2.1 Comparison and numerical and experimental result

The numerical and experimental results of a 75ppm CTAC solution are compared with those of water at a Reynolds number around 12000 as shown in Figs. 16-19.   Figure 16 shows numerically and experimentally that the addition of surfactant additives dramatically decreases the mean velocity in the viscous sub-layer, upshifts velocity profile in the logarithmic layer and expands the buffer layer. Both the numerical and experimental results in Fig. 17 show that, with the addition of surfactant additives, the peak of u_{rms}^+ shifts to the bulk flow, u_{rms}^+ increases except the near wall region and v_{rms}^+ decreases appreciably. The experimental reduction of Reynolds shear stress was reproduced by the numerical simulation as shown Fig. 18. The numerical simulation shows that the decrease of the Reynolds shear stress is due to the increase of the viscous shear stress and the induced positive viscoelastic shear stress, with a larger effect from the latter. The viscoelastic stress is the largest component in the near-wall region, where the Reynolds shear stress decreases most appreciably, indicating that a small amount of additives greatly change the balance of the shear stress. Figure 19 compares the budget terms of turbulent kinetic energy for Newtonian fluid and CTAC surfactant solution. The calculated production rates are in good agreement with the measured ones for both Newtonian fluid and CTAC surfactant solution. The magnitudes of the budget terms significantly decrease with the addition of surfactant additives. The turbulence-elasticity interaction acts as a strong sink-term along the channel height. The positions, where

production rate reaches its maximum value, molecular diffusion and turbulence diffusion reach their minimum values, shift towards to the bulk flow region. These shifts are consistent with the expansion of the buffer layer and show the effect of the surfactant additives on turbulence flow is primarily in the buffer layer.

3.2.2 Budget of momentum transfer

By expansion of FIK integration (Fukagata et al. 2002) to surfactant solution, the friction factor is decomposed into a viscous contribution, turbulent contribution, and viscoelastic contribution [4]. Figure 20 shows that surfactant additives have dual effects on frictional drag to: (1) introduce viscoelastic shear force, which has the function to increase frictional drag; and (2) decrease Reynolds shear stress to decrease frictional drag. The drag-reduction occurs because the second effect is the major effect.

3.2.3 Quadrant analysis

The effects of rheological parameters are studied. Numerical simulations show that drag-reduction rate increases with the increase of We_τ, with the decrease of α and with the increase of β. Large drag-reduction rate is associated with larger-size streamwise vorticity, larger elastic energy in the buffer layer and stronger reduction of burst events as shown in Fig.21. The stretching of the streamwise vortex is greatly reduced for a large drag-reduction rate. Figure 22 shows the quadrant analysis of the Reynolds shear stress. It is seen that the addition of surfactant additives primarily suppress the Q2 (ejection) and Q4 (sweep) motions. A bi-layer model shows clearly that surfactant additives are most effective in the buffer layer in reducing frictional drag (Yu B and Kawaguchi Y, 2004b).

3.2.4 Heat transfer analysis

Heat transfer reduction of a dilute CTAC surfactant solution was simulated. Some results are shown in Fig. 23. Figure 23 (a) shows that the addition of surfactant additives activates the temperature fluctuation and shifts its peak to the bulk flow region. Figure 23 (b) shows that the streamwise turbulent heat flux becomes larger with surfactant additives and its peak shifts to the bulk flow region. The significant increase of the streamwise heat flux is primarily owing to both the increase of the streamwise velocity fluctuation and the increase of the temperature fluctuation. The wall-normal turbulent heat flux with surfactant additives decreases as shown in Fig. 23(c). The suppressed wall-normal velocity fluctuation and the less cross-correlation between v' and θ' are the cause of the decrease of wall-normal heat flux. For surfactant solution, there is an increase of the conductive heat flux to compensate for the decrease of wall-normal heat flux as shown in Fig. 23(c), which means conduction plays a more important role in heat transportation with surfactant additives. The decrease of eddy diffusivities of momentum and heat with surfactant additives is seen in Fig. 23(d), indicating a less frequent and weaker turbulent transportation in the heat and fluid flow process. All these characteristics are qualitatively in agreement with the experiments.
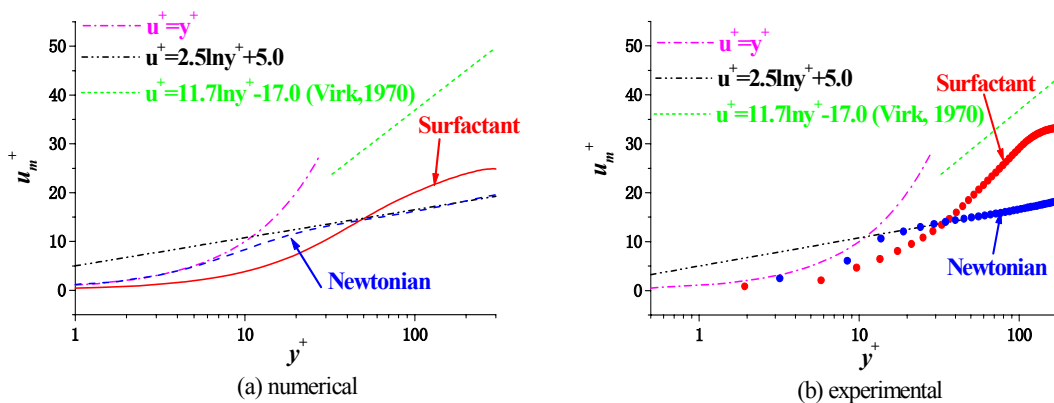
Figure 16 Comparison of mean velocity profiles for water and 75 ppm CTAC solution at Re=12000.
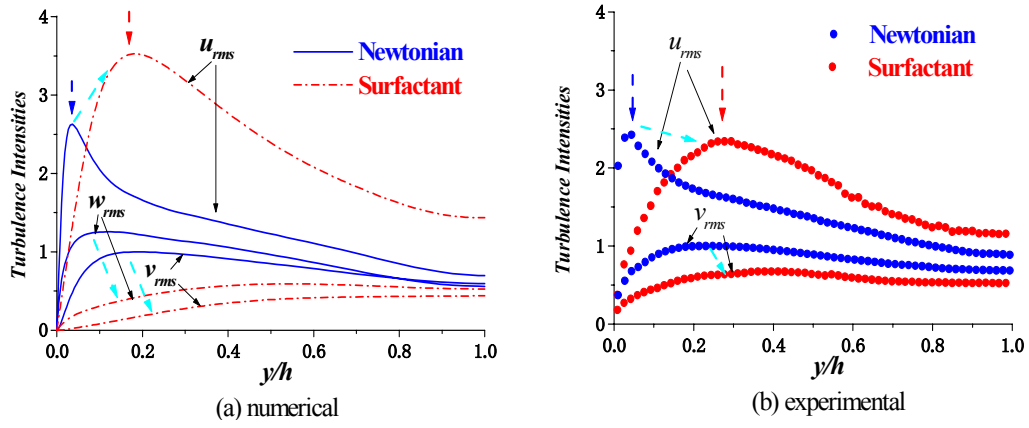
Figure 17 Comparison of RMS of velocity fluctuations for water and 75 ppm CTAC solution at Re=12000.
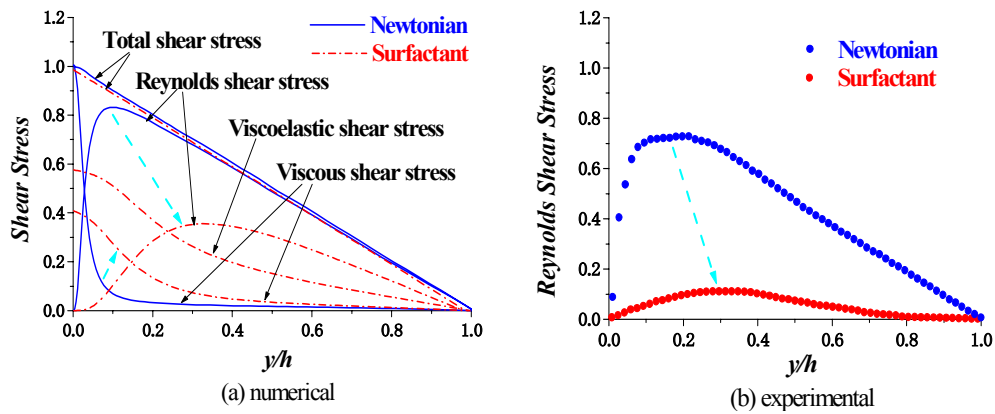
Figure 18 Comparison of Reynolds shear stress for water and 75 ppm CTAC solution at Re=12000.
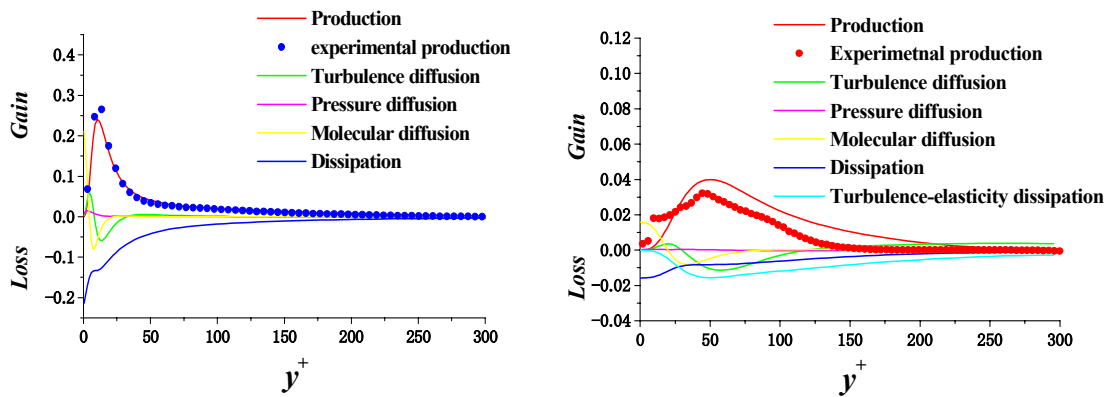
Figure 19 Comparison of turbulent kinetic energy budgets for water and 75 ppm CTAC solution at Re=12000.

Figure 20 The contributions to the friction factors for water and 75 ppm CTAC solution at Re=12000.

11
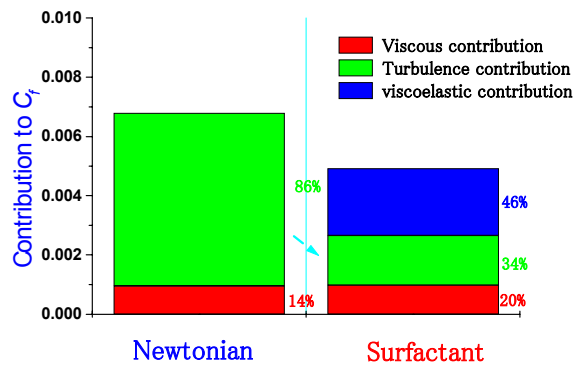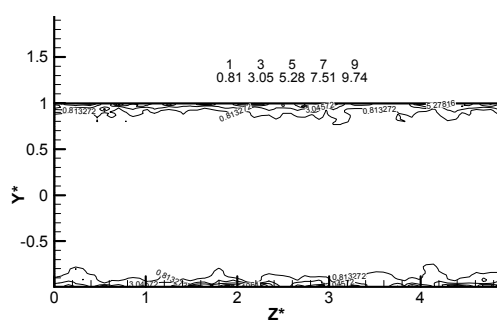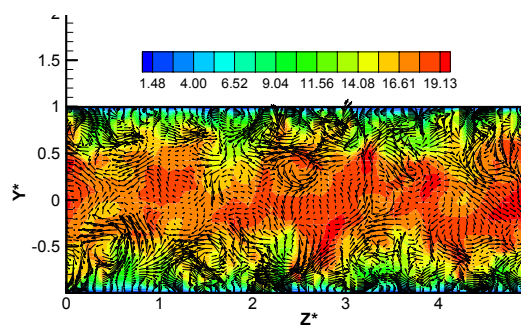
(a) DR%=0
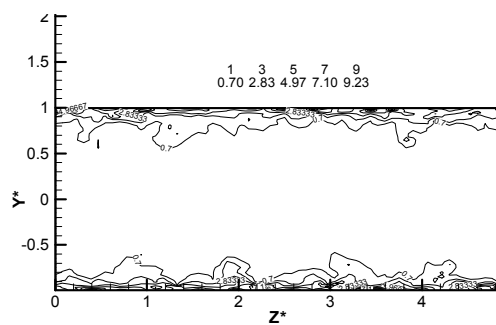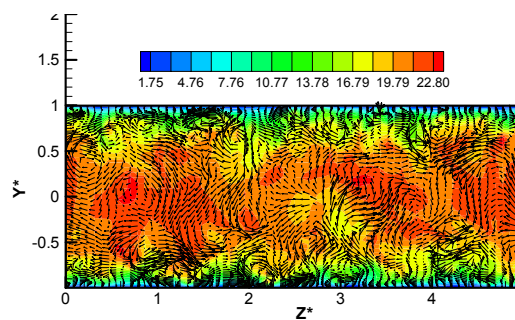
(b DR%=25.4%
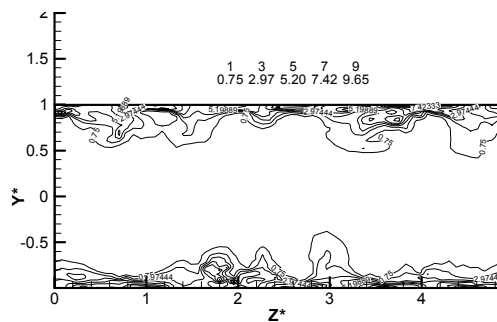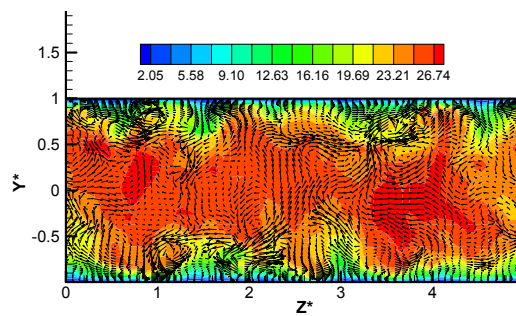
(c)DR%=46.0%
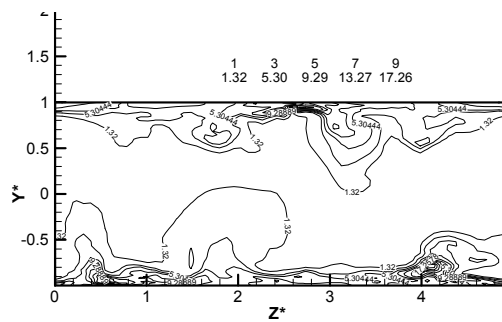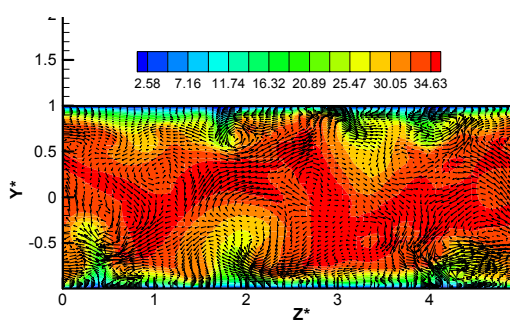
(d)DR%=67.7%

Figure 21 Instantaneous velocities and elastic energy at a y-z plane at different drag-reduction rates

(a) contour of streamwise velocity and v and w velocity vectors and (b) elastic energy
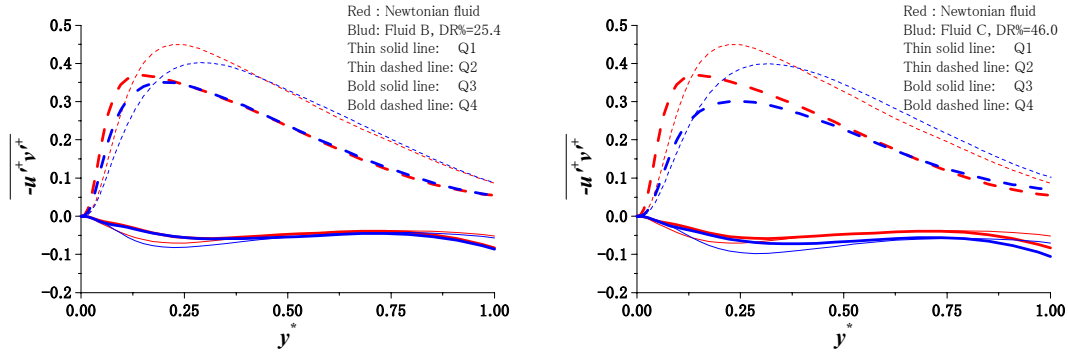
Figure 22 Reynolds shear stress from each quadrant
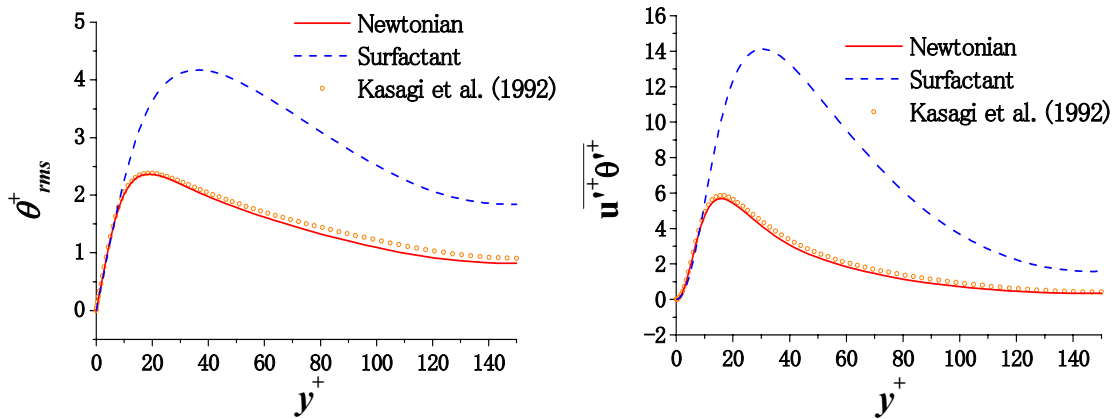
(a) RMS of temperature fluctuations

(b) streamwise turbulent heat flux
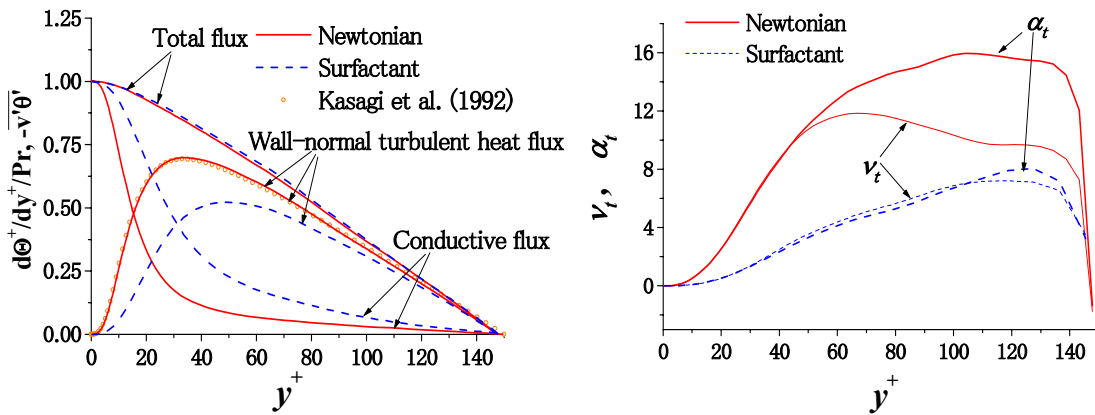
(c) Budget of heat flux

(d) Eddy diffusivities

Figure 23 Some results of heat transfer simulation

4. Conclusions

Turbulence structures and turbulence transport for momentum and heat in drag-reducing surfactant solution flows were experimentally and numerically investigated by means of Laser measurement techniques and DNS. The mechanisms of drag reduction and heat transfer reduction of drag-reducing surfactant solution flow, the characteristics of near-wall coherent turbulence structures and overall turbulence statistics influenced by drag-reducing additives and the relationship between skin friction and turbulent bursting events in a wall-flow, have been intensively studied and made clear.

References

Fukagata K, Iwamoto K and Kasagi N, 2002, Contribution of Reynolds stress distribution to the skin friction in wall-bounded flows. Phys. Fluids 14(11), L73-76.

Hu, Y. and Matthys, E.F. 1997 Evaluation of micellar overlapping parameters for a drag-reducing cationic surfactant system: Light scattering and viscometry. Langmuir 13, 4995.

Hu, Y.T., Boltenhagen, P. and Pine, D.J. 1998a Shear thickening in low-concentration solutions of wormlike micelles. I. Direct visualization of transient behavior and phase transitions. J. Rheol. 42, 1185.

Hu, Y.T., Boltenhagen, P., Matthys, E. and Pine, D.J. 1998b Shear thickening in low-concentration solutions of wormlike micelles. II. Slip, fracture, and stability of the shear-induced phase. J. Rheol. 42, 1209.

Kawaguchi, Y., Segawa, T., Feng, Z.-P. and Li., P.-W. 2002 Experimental study on drag-reducing channel flow with surfactant additives – spatial structure of turbulence investigated by PIV system. Int. J. Heat Fluid Flow 23, 700.

Li, F.-C., Wang, D.-Z., Kawaguchi, Y. and Hishida, K. 2004a Simultaneous measurements of velocity and temperature fluctuations in thermal boundary layer in a drag-reducing surfactant solution flow. Exp. Fluids 36, 131.

Li, F.-C., Kawaguchi, Y. and Hishida, K. 2004b Investigation on the characteristics of turbulence transport for momentum and heat in a drag-reducing surfactant solution flow. Phys. Fluids 16, 3281.

Li, F.-C., Kawaguchi, Y. and Hishida, K. 2004c Structural analysis of turbulent transport in a heated drag-reducing channel flow with surfactant additives. Int. J. Heat Mass Transfer, in print.

Li, F.-C., Kawaguchi, Y., Segawa, T. and Hishida, K. 2004d Experimental study on turbulent structure in drag-reducing surfactant solution channel flow – Reynolds number dependence –. *Recent Advances in Fluid Mechanics*, Ed. Zhuang, F. and Li, J., Tsinghua Univ. Press & Springer, 810.

Li, F.-C., Kawaguchi, Y., Segawa, T. and Hishida, K. 2004e Influence of drag-reducing surfactant additives on vortex structures and turbulent events in a channel flow. Proc. ASME HT-FED 2004, Charlotte, USA.

Li, F.-C., Kawaguchi, Y., Segawa, T. and Hishida, K. 2004f Characteristics of low-speed streaks and vortex structures in drag-reduced turbulent channel flow investigated by stereoscopic PIV. Symp. Rheol. Fluid Mech. Nonlinear Materials, IMECE, Anaheim, USA.

Li, P., Kawaguchi, Y. and Yabe, A. 2001a Transitional heat transfer and turbulent characteristics of drag-reducing flow through a contracted channel. J. Enhanced Heat Transfer 8, 23.

Li, P., Kawaguchi, Y., Daisaka, H., Yabe, A., Hishida, K. and Maeda, M. 2001b Heat transfer enhancement to the drag-reducing flow so surfactant solution in two-dimensional channel with mesh-screen inserts at the inlet. J. Heat Transfer 123, 779.

Lu, B., Li, X., Scriven, E., Davis, H.T., Talmon, Y. and Zakin, J.L. 1998 Effect of chemical structure on viscoelasticity and extensional viscosity of drag-reducing cationic surfactant solutions. Langmuir 14, 8.

Sureshkumar R, Beris AN and Handler R A, 1997 Direct numerical simulation of turbulent channel flow of a polymer solution. Phys. Fluids 9, 743-755.

Yu, B. and Kawaguchi, Y. 2003 Effect of Weissenberg number on the flow structure: DNS study of drag-reducing flow with surfactant additives. Int. J. Heat Fluid Flow 24, 491.

Yu, B. and Kawaguchi, Y. 2004a Direct numerical simulation of viscoelastic drag-reducing flow: a faithful finite difference method. J. Non-Newtonian Fluid Mech. 116, 431.

Yu B and Kawaguchi Y, 2004b, DNS of drag-reducing turbulent channel flow with coexisting Newtonian and Non-Newtonian fluid, ASME Heat Transfer/Fluids Engineering Summer Conference, Charlotte, North Carolina, USA, July 11-15.

Yu B, Li FC and Kawaguchi Y, 2004, Numerical and experimental investigation on turbulence characteristics in a drag-reducing flow with surfactant additives, International Journal of Heat and Fluid Flow, 25(6): 961-974 2004, 2004

Yu, B., Li, F.-C. and Kawaguchi, Y. 2004 Numerical and experimental investigation of turbulent characteristics in a drag-reducing flow with surfactant additives. Int. J. Heat Fluid Flow, in print.

Zakin, J.L., Myska, J. and Chara, Z. 1996 New limiting drag reduction and velocity profile asymptotes for nonpolymeric additives systems. AIChE J. 42, 3544.